

Numerical Framework for the Development of Atmosphere-Breathing Electric Propulsion for Earth and Mars Atmosphere

IEPC-2024-289

*Presented at the 38th International Electric Propulsion Conference, Toulouse, France
June 23-28, 2024*

V. Pessina* and J. Schein†

Bundeswehr University Munich, Neubiberg, 85577, Germany

M. Smirnova‡

TransMIT GmbH, Gießen, 35390, Germany

Abstract: Atmosphere Breathing Electric propulsion systems can provide a competitive advantage since the primary working fluid is directly collected from the atmosphere. This technology operates best at lower altitudes, where the atmospheric gas is dense enough to provide a reasonable collected mass flow. The characterization of collection and compression performances and drag to compensate is crucial for this technology feasibility and development. To begin with, the atmospheric characterization based on NRLMSISE-00 for Earth and several mission data for Mars is derived for the lower altitude ranges of interest. This characterization provides a reliable dataset of boundary conditions for the simulations in the second part of this study, in which a computational framework based on the Direct Simulation Monte Carlo method is presented with the aim to investigate the collection and compression performance and drag estimation. The computational setup is validated by a numerical comparison with a literature case. For this simplified geometry, the impact of the gas-surface interaction modelling is investigated for a VLEO altitude of 180 km. The main investigated gas-surface interaction models are the fully specular, and partially diffuse reflection described by the Maxwellian model first, and then the Cercignani-Lampis-Lord model with both isotropic and anisotropic scattering kernel. Since at the inlet of the ionization stage the intermolecular collisions become more relevant, the impact of both the Variable Hard and Soft Sphere models is investigated, as well as a brief discussion on the inclusion of gas-phase reactions. Finally, the simulation results of the two cases for the low Mars orbit (150 and 140 km) are discussed.

Nomenclature

ABEP	= Atmosphere Breathing Electric Propulsion
AETHER	= Air-breathing Electric ThrustER
CLL	= Cercignani Lampis Lord
DSMC	= Direct Simulation Monte Carlo
GSI	= Gas-surface Interaction
LEO	= Low Earth Orbit

*Post-Doc. Researcher, Institute of Physics and Plasma Technologies, valentina.pessina@unibw.de.

†Professor, Institute of Physics and Plasma Technologies.

‡Project Division Director, TransMIT IQM.

MABHET	= Martian atmosphere breathing Hall effect thruster
MAVEN	= Mars Atmosphere and Volatile EvolutioN
NGISM	= Neutral Gas and Ion Mass Spectrometer
RPA	= Retarder Potential Analyzer
S/C	= Space Craft
SPARTA	= Stochastic PARallel Rarefied-gas Time-accurate Analyzer
TCE	= Total Collision Energy
UAMS	= Upper Atmosphere Mass Spectrometer
VHS	= Variable Hard Sphere
VLEO	= Very Low Earth Orbit
VSS	= Variable Soft Sphere
A_{ioniz}	= area of the cross section of the ionization stage
A_{ref}	= reference area for aerodynamic drag
c_d	= drag coefficient
D	= atmospheric drag force
d_{ref}	= reference diameter for particle collision
E_i	= kinetic energy of the incident particle
E_r	= energy of the re-emitted particle
E_w	= energy the particle needs to deplete to reach thermal equilibrium with the wall
h	= altitude
k_B	= Boltzmann constant
Kn	= Knudsen number
L_c	= characteristic length for the Knudsen number
L_{cell}	= computation grid cell dimension
m_p	= mass of the particles
MW_{ave}	= average molecular weight of atmospheric mixture at a given altitude
n	= number density
n_{tot}	= total number density
N_A	= Avogadro number
p	= pressure
R	= ideal gas universal constant
r_{ref}	= reference diameter of the ionization stage
s	= speed ratio
x_i	= mole fraction of species i
v	= velocity
v_b	= bulk velocity
v_{orb}	= orbiting velocity of the satellite
$v_{thermal}$	= thermal velocity
α	= exponent of the VSS and VHS molecular models
α_{acc}	= accommodation coefficient
$\alpha_{acc,n}$	= accommodation coeff. in the normal direction
$\alpha_{acc,rot}$	= accommodation coeff. for the rotational energy
$\alpha_{acc,t}$	= accommodation coeff. in the tangential direction
$\alpha_{acc,vib}$	= accommodation coeff. for the vibrational energy
λ	= molecular mean free path
ρ	= mass density
ω	= temperature exponent in the viscosity calculation for the molecular models

I. Introduction

THE main innovative idea behind Atmosphere Breathing Electric Propulsion (ABEP) systems is that the propellant is directly collected from the atmosphere. An intrinsic theoretical advantage of this technology is that an on-board fuel tank is not strictly required, and consequently the life time of the satellite mission powered by ABEP can be extended, provided a durable plasma generation source, with a reduced tendency to erosion and wear down. Several concepts were presented as reported in several recent review studies¹⁻³ and less recent works,^{4,5} both targeting Low Earth Orbits (LEO) and Very Low Earth Orbits (VLEO) with projects such as the ESA RAM-EP,⁵ the studies in collaboration with JAXA,^{6,7} the Air-breathing Electric THRuster (AETHER)⁸ project, or the different designs proposed by universities,⁹⁻¹¹ and finally the proposal for Mars in the Martian Atmosphere Breathing Hall Effect Thruster (MABHET).⁴ Generally, the ABEP systems target lower orbits, where the atmosphere is dense enough to provide an adequate mass flow rate, which is determined by the thrust required to prevent unplanned deorbiting. The low-orbit target is an additional advantage in terms of launch costs.¹² However, at lower orbits, the increased aerodynamic drag experienced by the spacecraft (S/C) demands a thrust capable of a full compensation, hence the crucial effective collection of atmospheric particle. From the schematics shown in Fig.1, one can split the design of ABEP into three main strategic steps: first the characterization of the *fuelling propellant*, hence the knowledge of the available atmospheric gas, second the design of an effective intake-compression-thermalization stage, which should be designed based on the *rarefied gas-dynamics*, and finally an efficient *electric thruster* where the gas is ionized and accelerated based on the selected propulsion system principles. Although these three aspects are inherently connected, this paper focuses on the first two parts aiming to provide a numerical framework for the design of the intake for both Earth and Mars atmosphere. The use of the rarefied gas-dynamics¹³ and the Direct Simulation Monte Carlo (DSMC) method¹⁴ are the essential base employed in this study to tackle the design of ABEP systems, since it can provide estimation of the drag to be compensated by the thrust, as well as the information regarding the intake design. The DSMC-simulation has proven to be an effective tool for intake design purposes as shown in several Earth-related studies targeting VLEO applications, such as the comparison of different intake designs¹¹ targeting the Earth orbital altitudes from 150 km to 250 km with PIC-DMSC-code PICLas,¹⁵ or the comparison of different inlet duct patterns with the help of dsmcFoam+,¹⁶ or the inlet flow simulations of ABEP systems with SPARTA (Stochastic PARallel Rarefied-gas Time-accurate Analyzer) DSMC-solver.¹⁷⁻¹⁹ These studies offer a detailed methodology for the geometric intake design for Earth applications, with more or less complex Gas-Surface interaction (GSI) description, whereas DSMC simulations for Martian applications are rare to be found in the literature.

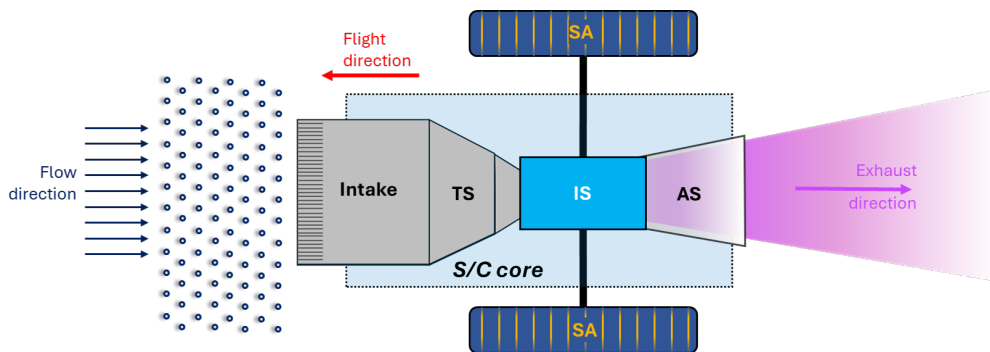


Figure 1: Schematics of ABEP system: intake, thermalization stage (TS), ionization stage (IS), acceleration stage (AS), solar array (SA), and spacecraft (S/C) core.

This study aims to apply the DSMC-based simulations for the ABEP system development with the actual conditions experienced by the orbiting satellite, to estimate the key parameters for the ABEP design, such as the compression performances, the mass flux to the thruster, and a final remark on the aerodynamic drag D . After providing the atmospheric characterization for Earth (120 km to 260 km) and Mars (100 km to 200 km), the numerical framework is applied to a VLEO case at 180 km, and low Mars orbit at 140 and 150 km altitude.

For a simplified geometry from literature,¹⁸ the impact of the GSI modelling is investigated for the Earth case by comparing simulation results from specular to partial and total diffuse reflection based on the Maxwellian model,²⁰ as well as the Cercignani-Lampis-Lord model,^{21,22} which assumes that the reflected particles have a lobular distribution. A brief check on the impact of the model for the intermolecular collision is carried out with Variable Hard Sphere (VHS) and with Variable Soft Sphere (VSS), since after the compression the mean free path between the particles decreases compared to the one from the free molecular flow around the S/C. Finally, the application to the Mars atmosphere is presented with a comparison drawn for the collection and compression performances, as well as for the drag.

II. Methodology

A. Atmospheric characterization

The aim of the atmospheric characterization is to describe the variation with the altitude of the gas properties such as density and temperature as well as the composition, which are the boundary conditions for the ABEP systems simulations and operation. In this study, the characterization is achieved for a wide low-altitude range for both Earth (120 km to 260 km) and Mars (100 km to 200 km). First, the published information from previous missions and atmospheric models is gathered and compared, then the values of temperature, density, and composition are interpolated to build database with 10 km stepping. This way, the values can be compared for a given altitude thanks to the customized altitude stepping obtained with the interpolation. The reference for Earth atmospheric characterization is the NRLMSISE-00 model.^{23,24} As for Martian atmosphere, the data from several missions are compared. The temperature is extracted from the data provided by the Viking 1 and 2 landers.^{25,26} The characterization of the mass density variation with the altitude is crucial for determining the performance of the ABEP systems for a given orbit altitude, since the density directly impact both the aerodynamic drag force experienced by the satellite ($D/A_{ref} \propto \rho C_d v_{orb}^2$) and the mass flow rate to the ionization and acceleration stage, hence the obtainable thrust. The density data from different Mars missions are compared in Fig.2: the fitting function proposed by Blanchard based on the reentry measurements of Viking 1 lander,²⁷ the data from Mars-GRAM 2000,²⁸ and the Pathfinder.²⁹

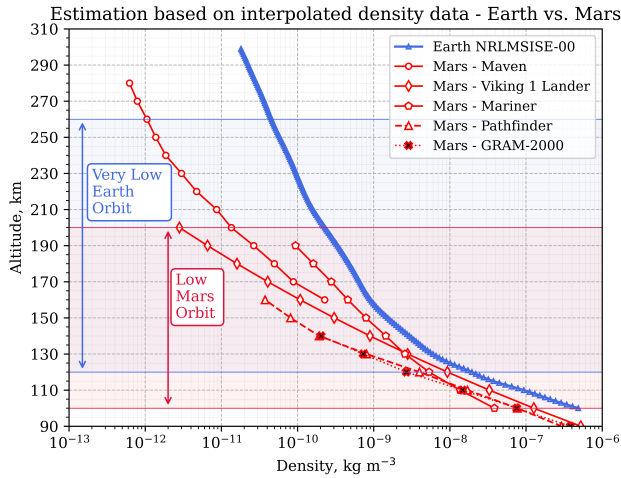


Figure 2: Density with altitudes: data from NRLMSISE-00 for Earth, for Mars the comparison between different missions.

The density for the data from Mars Atmosphere and Volatile EvolutionN (MAVEN) and Mariner 9 is reckoned in this study based on the ideal gas law and the total number density. As a first approximation of the total number density, the charged particles are neglected in the sum, since they have a number density ranging from 10^6 to 10^{11} m^{-3} compared to the one of the neutrals, which ranges between 10^{14} to 10^{18} m^{-3} (example at 100 km). From the total number density n_{tot} , the mole fraction x_i of each species i , the average molecular weight is estimated based on a mole-based average, and finally the mass density of the atmospheric gas is reckoned based on the ideal gas assumption as per Eq.(1):

$$\rho = (n_{tot} MW_{ave}) / N_A \quad (1)$$

The temperature and density of Earth and Mars for low orbits are compared in Fig.3, whereas the density comparison between the aforementioned Martian missions is summarized in Fig.2.

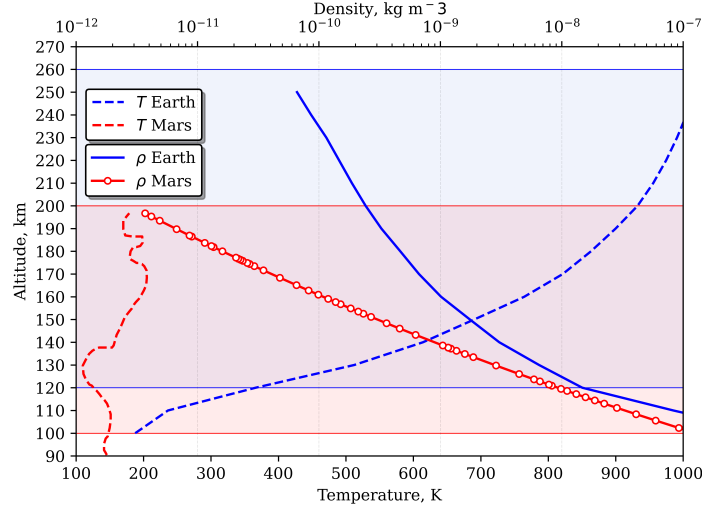


Figure 3: Variation of temperature and density with the altitude. The altitude range of interest are highlight in red for Mars, in blue for Earth.

As for the atmospheric composition, the ultraviolet spectrometer observations, airglow measurements from Mariner 9 mission (100 km to 200 km) are collected^{30,31} as initial set of data. A second dataset is derived from the measurements during the descendant of the Viking 1 lander (1976), which was equipped with the Upper Atmosphere Mass Spectrometer (UAMS) and a Retarder Potential Analyzer (RPA).³² The third dataset for the composition is reckoned from the more recent observations by MAVEN from 155 km to 200 km³³ and for lower altitude.³⁴ In Fig.4b) the composition of the main 9 species (CO₂, CO, NO, N, N₂, O₂, O, Ar, He) derived from the MAVEN observations. As for Earth, the NRLMSISE-00 model is consistently taken as a reference and the neutral number density values for the main 7 species (N₂, N, O₂, O, Ar, He, H) is drawn in Fig.4a).

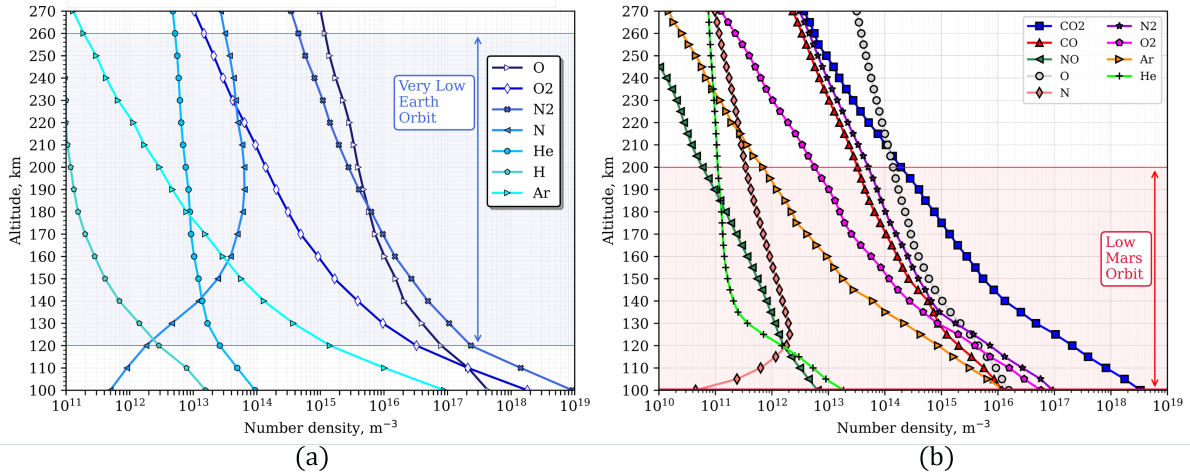


Figure 4: Earth atmospheric composition from NRLMSISE-00 (a). Mars atmospheric composition: data from NGISM-Maven (b).

B. Direct Simulation Monte Carlo Method and simulation setup

The DSMC method¹⁴ provides a stochastic description of a representative population of particles based on the Boltzmann equation for the gas kinetics. For each particle, the instantaneous values of the properties of interest are then averaged to obtain a statistically relevant description. Finally, the macroscopic fluid properties can be estimated as the average of the values assumed by the set of particle belonging to a given computational cell. The DSMC method is suitable for rarefied gas dynamics problems since it is effective for both the transitional flow regime ($0.1 \leq Kn \leq 10$) and the free molecular flow regime ($Kn > 10$). The flow regime can be identified based on the Knudsen number (Kn), which is generally defined as the ratio of the molecular mean free path λ and the characteristic length of the problem L_c . For the free-stream, the value of λ in Eq.(2) varies with the altitude (Fig.5), since both n_{tot} and the reference diameter d_{ref} , which for the mixture is the average value based on the composition analogously to the MW_{ave} .

$$\lambda = \frac{k_B \cdot N_A}{\sqrt{2} \cdot \pi \cdot R} \cdot \frac{1}{d_{ref}^2 \cdot n_{tot}} \quad (2)$$

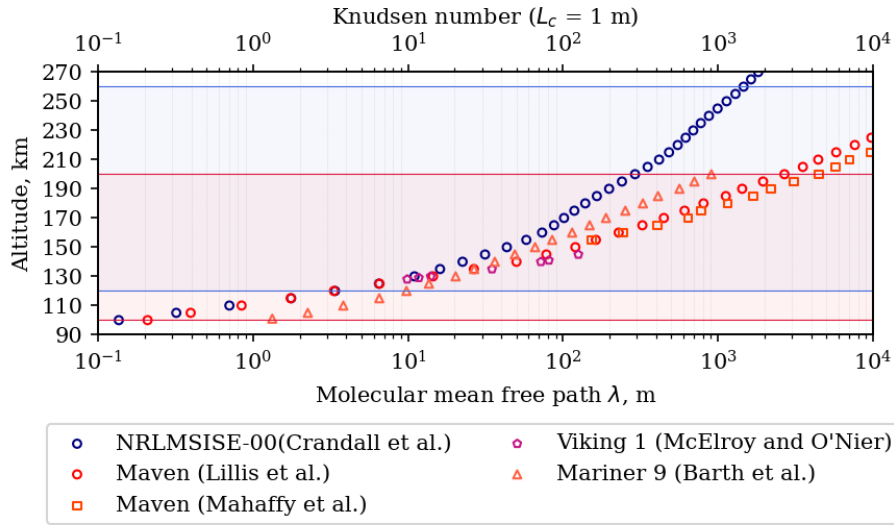


Figure 5: Free-stream conditions: variation with the altitude of the molecular mean free path (λ) and Knudsen number (Kn) in case of characteristic length L_c of 1 m.

As the definition suggests, the Kn varies also with the selected L_c , which can be set equal to the intake inlet diameter (~ 1 m) or the ionization stage inlet diameter (~ 0.08 m), hence for this reason, λ is preferred for the grid size definition. Once the altitude of interest for a DSMC simulation is selected, λ is uniquely determined by n_{tot} and average d_{ref} , and from this information the computational grid dimension L_{cell} can be set accordingly to this constrain: $L_{cell}/\lambda \ll 1$. In the same fashion of λ and Kn , the speed ratio s Eq.(3) can shed light on the more relevant collision phenomena.

$$s = \frac{v_b}{v_{thermal}} = \frac{v_b}{\sqrt{\left(\frac{2 \cdot T \cdot k_B}{m_p}\right)}} \quad (3)$$

In case of hypersonic flows ($s > 5$) the Brownian motions are less relevant than the the surface-particle collisions, making the GSI modelling a priority over the intermolecular collision model, vice versa for thermal flow ($s \sim 1$), where the random molecular motion becomes more relevant than the collective motion. In case of ABEP, the free-stream flow is in hypersonic conditions, then the particles start to collide with the surface, partially being reflected, partially being collected in the intake, where the Brownian motions and random collisions result in a thermalization of the flow, which slows down, thus providing a compression effect. In light of these observations, both GSI and inter-particle collision are relevant and their accurate modelling is necessary. The inter-particle collisions and the anisotropic scattering is described with both the

Variable Hard Sphere (VHS) and the Variable Soft Sphere (VSS). The input parameters for the VHS model shown in Table 1 are derived from,^{14,35} whereas the VSS model parameters are taken from the more recent work by Pfeiffer et al.³⁶

Table 1: VSS and VHS parameters for modelling the inter-particle collisions.

Species	mass (kg)	VHS			VSS		
		ω (-)	d_{ref} (m)	α (-)	ω (-)	d_{ref} (m)	α (-)
O ₂	5.310×10^{-26}	0.77	3.96×10^{-10}	1.00	0.702	3.773×10^{-10}	1.391
N ₂	4.650×10^{-26}	0.74	4.07×10^{-10}	1.00	0.693	3.911×10^{-10}	1.351
O	2.650×10^{-26}	0.80	3.00×10^{-10}	1.00	0.772	3.340×10^{-10}	1.471
N	2.325×10^{-26}	0.80	3.00×10^{-10}	1.00	0.753	3.402×10^{-10}	1.477
NO	4.980×10^{-26}	0.79	4.20×10^{-10}	1.00	0.716	3.983×10^{-10}	1.425
CO ₂	7.310×10^{-26}	0.93	5.62×10^{-10}	1.00	0.693	4.647×10^{-10}	1.37
CO	4.650×10^{-26}	0.73	4.19×10^{-10}	1.00	0.726	4.101×10^{-10}	1.34
Ar	6.630×10^{-26}	0.81	4.17×10^{-10}	1.00	0.700	3.832×10^{-10}	1.384

As the inter-particle collisions, the particle-surface collision description is analogously important. In this study, different descriptions are compared in terms of compression effect due to thermalization. After the intake, the collected particles slow down as a consequence of the repeated collisions with the surrounding surfaces, hence the collected rarefied gas is thermalized and subject to compression. The most popular GSI model for the calculation of post-collision kinetic energy is the partially diffuse reflection by Maxwell,^{14,20} in which only a fraction of the impinging particles are specularly reflected, while the remaining are fully accommodated (complete diffuse reflection), depending on the value of the accommodation factor α_{acc} described in Eq.(4).

$$\alpha_{acc} = \frac{E_i - E_r}{E_i - E_w} \quad (4)$$

The accommodation coefficient can vary between one and zero. The null value indicates the totally specular reflection in which the pre- and post-collision kinetic energy of the particle is unchanged after the specular reflection. In case of α_{acc} equal to unity, the totally diffuse reflection occurs, and the post-collision particle is in thermal equilibrium with the wall. However, as demonstrated by Cercignani and Lampis,²¹ a more realistic reflection pattern for a molecular beam is described by a lobular distribution in direction of the re-emitted particle velocity vectors. Unlike the Maxwellian model, two post-collision characteristic temperatures of the reflected particles are defined: one for the scattering kernel of the tangential velocity, and one for the kernel of the normal velocity. The modification of this model done by Lord includes the diffuse scattering with partial energy accommodation, and also the vibrational accommodation.²² The Cercignani-Lampis-Lord (CLL)^{21,22} model as implemented in the SPARTA DSMC solver³⁵ allows the use of different accommodation coefficients: a coefficients for the accommodation in the tangential direction and one for the normal direction ($\alpha_{acc,t}$ and $\alpha_{acc,n}$), then one for the vibrational and rotational energy accommodation ($\alpha_{acc,vib}$ and $\alpha_{acc,rot}$ respectively). In this study, the results yielded by the GSI modelling with specular, diffuse, and partially diffuse scattering with the Maxwellian model is compared with the results yielded by the CLL GSI model. Finally, for the test case in Earth atmosphere, the role of the reactions within the gas phase is investigated. For the Total Collision Energy (TCE), set of reactions for the Earth's species is set based on the results reported by the NASA study.³⁷ In this study, the aim of the DSMC simulations is to investigate and characterize the flow parameters of the intake of a simplified geometry, such as mass and number density, and pressure, and eventual indications of the intake capabilities.

C. Computational domain and grid

The simplified slope geometry proposed by¹⁸ is shown in a 3D cut section in Fig.6b), along with the schematization of the boundary conditions assigned to the computational domain in Fig.6a). The 2D axi-symmetric computational domain comprise an axi-symmetric boundary and an open boundary around the far-field, with one of them set as an equivalent in-flow boundary on which the number of particles and their velocity are set. The ABEP surface is set as a wall boundary, with a GSI model.

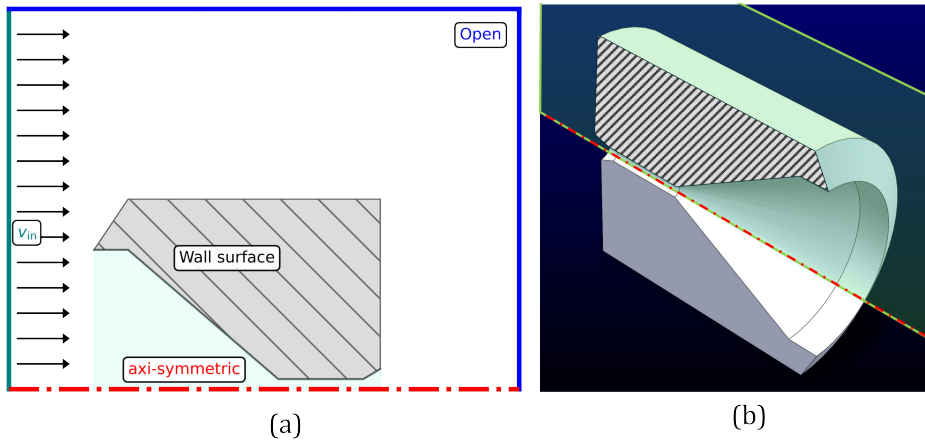


Figure 6: Computational domain schematics (a) with boundary conditions highlighted, and a 3D schematics of the simplified geometry .

The total extension of the domain is at least 6 times bigger than the total length of the ABEP ($L=1.7$ m) along the axi-symmetry axis direction, and at more that 4 time the max external radius of the ABEP (~ 0.75 m). The cartesian grid created for this study is the same for the Mars and Earth test cases, since its grid dimension satisfies the condition of $L_{cell}/\lambda \ll 1$ for both cases. More specifically, the estimation of L_{cell} is done based on the estimated d_{ref} at 180 km of the Earth atmosphere, and the average values of the local number density extracted from a first round of simulations serving the purpose of grid size definition before the final round of cases. A summary of the different values of L_{cell} for each level of the refinement is provided in Table 2. Beside the multi-level static refinement, for each case an adaptive refinement and coarsening is carried out to optimize the computational cost. The grid adaptation criterion is based on lower and higher threshold for the local value of n_{tot} , which is linked to λ in virtue of Eq.(2), and the final result is shown in Fig.7. The size simulation box size is 12 m along axi-symmetric axis (y axis), and 4 m in the orthogonal direction (x axis). The simulation timestep is set to 1×10^{-6} s, the total number of simulated particle is adjusted to have at least 20 particles per cell, even in the refined areas.

Table 2: Comparison between the grid cell size and the molecular mean free path for 180 km altitude of the Earth atmosphere.

Refinement Lev. →	Level 1	Level 2	Level 3	Level 4
L_{cell} →	0.1 m	0.05 m	0.025	0.0125

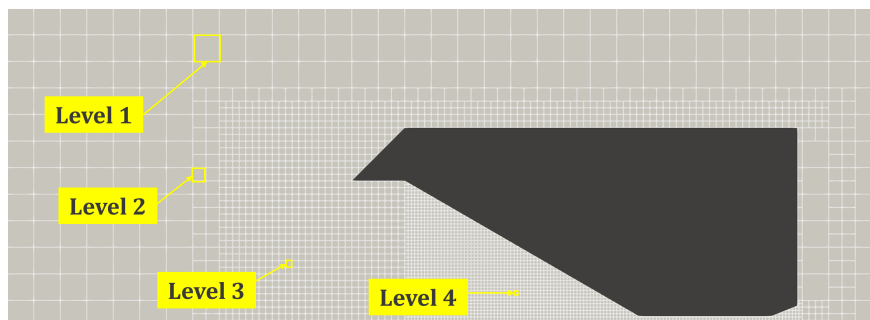


Figure 7: Grid detail: multi-level refinement of the cartesian grid, after the grid adaptation.

The reason behind the selection of this test-geometry from literature¹⁸ is two fold: first, a simple geometry is easier to handle for the numerical-to-numerical validation between the results discussed by¹⁸ and the ones from this study, and second the simplified geometry is a starting point to isolated the impact of the models on the estimation of the quantities of interest. However, whereas the analysis presented by¹⁸ focuses on the

inlet geometries with a Maxwellian GSI model, this study aims to investigate the different results yielded by different GSI models for a given geometry, adding the comparison with the CLL GSI model, to explore the eventual differences yielded by VHS and VSS, and finally to apply it to the case of the Martian atmosphere.

III. Results and discussion

The results for the simplified test geometry are reported in this section, starting with a numerical validation with the reference case from literature.¹⁸ Once the numerical setup (grid and models) are at least numerically validated, the compression and collection performances yielded by different GSI models are analyzed for the reference case for 180 km altitude of Earth atmosphere. Although less relevant if compared to the GSI model, the inter-particle collision model VHS and VSS are also compared, and additionally the impact of the gas-phase reactions is tested. Then, the application of this simple slope geometry is tested for Martian atmosphere at two altitudes 140 and 150 km.

A. Numerical setup validation

The numerical setup quality is assessed by the comparison with the reference case from literature,¹⁸ for the slope geometry and for boundary conditions relating to a VLEO orbit altitude of 180 km as summarized in Table 3.

Table 3: Boundary conditions for the Earth atmosphere cases corresponding to the free-stream conditions at 180 km altitude.

h (km)	ρ (kg m^{-3})	n_{tot} (m^{-3})	T (K)	p (Pa)	v_{in} (m s^{-1})	x_O (-)	x_{N_2} (-)	x_{O_2} (-)
180	5.198×10^{-10}	1.4×10^{16}	790	1.523×10^{-4}	7760	0.4820	0.4829	0.0351

The GSI model for the validation is the Maxwellian model with a partially diffuse reflection ($\alpha_{acc} = 0.5$). The intermolecular collisions are described with the VHS model, and the gas-phase reactions are neglected. The alignment of this study results and the reference case is achieved with a satisfactory agreement in terms of pressure values along the axi-symmetry axis and the gas mass flux through the selected cross-section at the entrance of the ionization stage (at a distance of 1.2 m from the intake inlet section). The values of the mass flux ($v \cdot \rho$) are reported in Fig.8a): the error is within 20% maximum for the majority of the points corresponding to the values in the radial direction of the cross section defined at 1.2 m of axial length (highlighted in red in Fig.8b)); the contour plots representative of the mass flux ($\text{kg} \cdot \text{m}^{-2} \cdot \text{s}^{-1}$) for the reference value of the accommodation coefficient ($\alpha_{acc}=0.5$) in Fig.8b) and for an increase in its value of 10% ($\alpha_{acc}=0.55$) in Fig.8c). The value of the pressure along the axi-symmetry axis is showed in Fig.9a) along with the case of $\alpha_{acc}=0.55$ in Fig.9b), as well as the number density in Fig.9c), and the maximum error is below 2%, and below 5% for the case $\alpha_{acc}=0.5$.

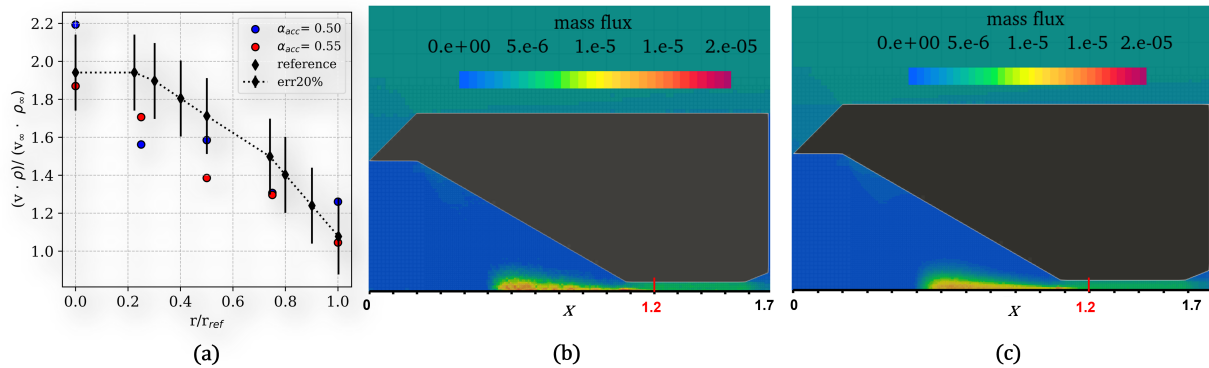


Figure 8: Result of mass flux ($\text{kg} \cdot \text{m}^{-2} \cdot \text{s}^{-1}$) evaluated at 1.2 m (section in red): values compared to the reference case (a) and contour plots for Maxwellian model with α_{acc} set to 0.5 (b) and 0.55 (c).

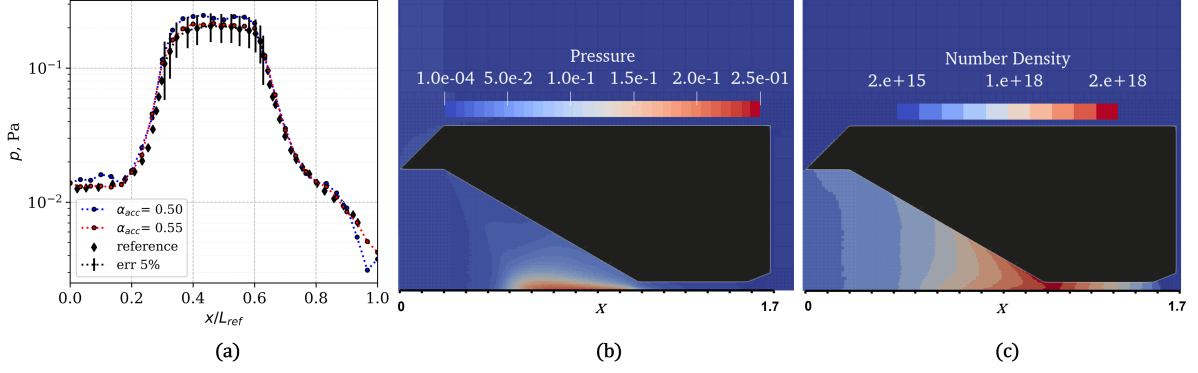


Figure 9: Result of pressure along the axi-symmetry axis direction (a) and contour plot of the pressure (b) and number density (c) for $\alpha_{acc} = 0.55$.

B. Performances in Earth atmosphere

The DSMC simulation results are discussed in terms of collection and compression performances of the simplified geometry for 180 km altitude in Earth atmosphere. The aim is to highlight the different results yielded by the GSI model (Specular, Maxwellian, and CLL) first, as well as the intermolecular collision models (VHS and VSS), which become more relevant between the thermalization and ionization stage due to the increased number density, generally two orders of magnitudes higher than in the free-stream. The 2D axi-symmetric simulations are carried out with the boundary conditions for summarized in Table 3, and each case is run with a specific setup to isolate the variation of collection and compression performances due to either the intermolecular collision, GSI, or gas-phase chemistry model. The cases and their simulation setup variation is listed in Table 4, with a composition based on the predominant species at 180 km altitude (O, O₂, N₂).

Table 4: Case setup summary for Earth atmosphere: the setup variations are encompassing intermolecular collision, gas-surface interaction, and gas-phase reactions.

Case ID	Case 1	case 2	Case 3	Case 4	Case 5	Case 6	Case 7
GSI model	Maxwell	Maxwell	Maxwell	Maxwell	Specular	CLL	CLL
α_{acc} (for Maxw.)	0.55	0.55	0.55	1.0	0.0		
α_n (for CLL)						0.55	0.55
α_t (for CLL)						0.55	0.75
Intermolecular collisions	VHS	VHS	VSS	VHS	VHS	VHS	VHS
Gas-phase reactions	none	TCE	none	none	none	none	none

The compression performance can be evaluated by the pressure values along the axi-symmetry line (Fig.10). The total length L of the ABEP along the axial direction is 1.7 m, and after 0.4 m from the intake inlet section (located at $x = 0$ m), the compression effect can be observed. The pressure increase is visible until the ionization section ($\sim 1 \div 1.2$ m), after which the pressure starts dropping. Compared to the free-stream pressure value of approximately 1.523×10^{-4} Pa, the compression effect results in a pressure increase up to 0.2 Pa for the Maxwellian partially diffuse reflection (α_{acc}), as well as for the lobular reflection with anisotropic scattering ($\alpha_n = 0.55$ and $\alpha_t = 0.75$), and slightly higher for lobular reflection with isotropic scattering. The pure specular reflection yields the highest value of pressure (~ 0.6 Pa), whereas the completely accommodated diffuse reflection ($\alpha_{acc} = 1.0$) with the Maxwellian description results in an less realistic pressure trend, which is stabilized along the axial direction. As for the collection performance, an indicator offered by the DSMC simulation is the mass flux ($v \cdot \rho$) and the mass flow rate ($v \cdot \rho \cdot A_{ioniz}$) evaluated at the ionization stage inlet section (~ 1.2 m). As for the mass flux (Fig.11), the Maxwellian model with $\alpha_{acc} = 0.55$ (case 1) results in values comparable to the ones from the anisotropic scatter with CLL (case 7). As expected, the highest values are yielded by a specular reflection, whereas the fully diffuse reflection results in the lowest.

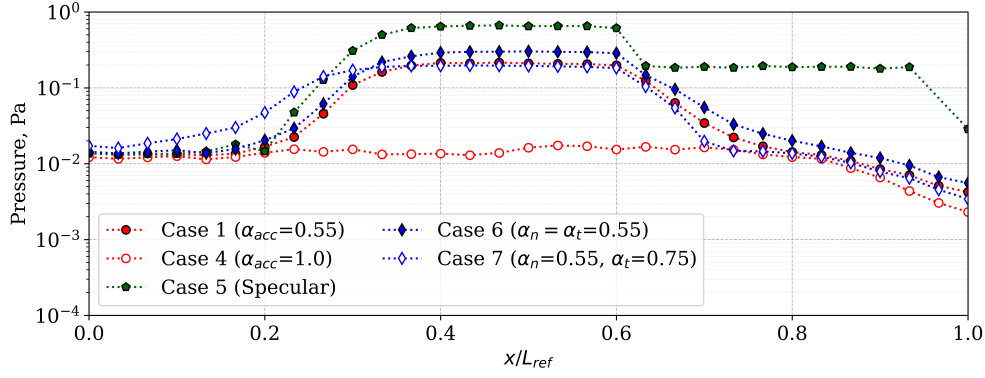


Figure 10: Values of the pressure along the center line for each case relating to Earth (Table 4). The total length L_{ref} is 1.7 m.

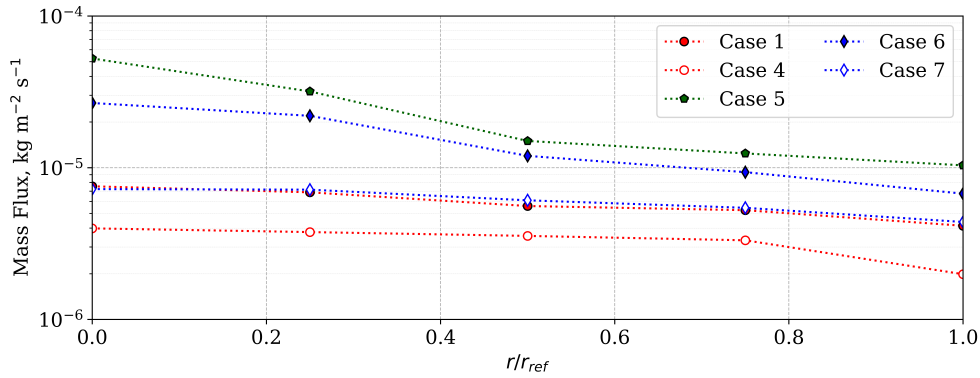


Figure 11: Mass flux values on the cross section of the ionization stage ($r_{ref} = 0.04m$) at 1.2 m from the intake inlet. For all cases, the intermolecular collision is modelled with the VHS, whereas the GSI varies from the Maxwellian model (red), specular (green), and lobular CLL (blue).

As for the differences due to the choice of VHS or VSS model are very limited for the altitude examined, both in terms of compression performance (Fig.12a) or mass flux (Fig.12b) and in number density contour plot (Fig.12c).

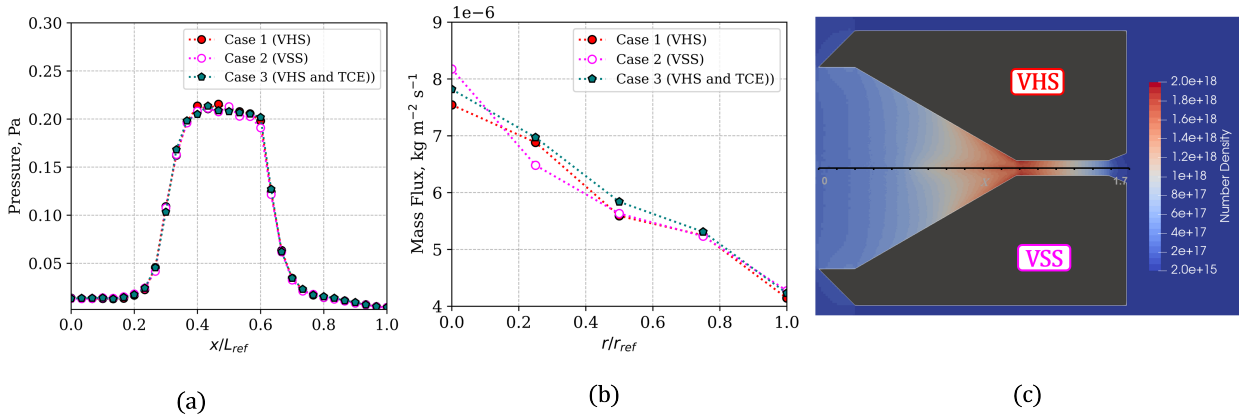


Figure 12: Results from VHS and VSS intermolecular collision models, and TCE for VHS. Pressure (a) and mass flux (b) with a linear scale; number density contour plot (c) for VHS (top) and VSS (bottom).

C. Performances in Mars atmosphere

The Martian atmosphere is investigated at two different altitudes, 140 km and 150 km, with VHS model, and a partially diffuse reflection with the Maxwellian model ($\alpha_{acc}=0.55$). The investigated altitudes are selected to match either the gas mass density of the VLEO at 180 km altitude (150 km), or the product of the mass density and the orbiting velocity, hence to match the theoretical mass flux at intake inlet ($\rho_{\infty} \cdot v$). For this case study, the ABEP orbits with no angle of attack, hence the velocity has a non-zero value only in the axial direction, which is estimated for Mars is 3400 m s^{-1} , which is $\sim 44\%$ less than the average orbiting velocity selected for the VLEO simulations. This results in a theoretical intake inlet mass flux of $\sim 3.75 \times 10^{-6} \text{ kg m}^{-2} \text{ s}^{-1}$ for Mars at 140 km altitude and $\sim 1.53 \times 10^{-6} \text{ kg m}^{-2} \text{ s}^{-1}$ at 150 km, compared to $\sim 4.03 \times 10^{-6} \text{ kg m}^{-2} \text{ s}^{-1}$ of the VLEO case at 180 km. The boundary conditions are extracted from the atmospheric characterization previously discussed, and the reference mission for density and composition is the MAVEN^{33,34} mission. The free-stream composition is set for each altitude as the six most relevant species with the higher volume fraction, as summarized in Table 5. The temperature reference for the free-stream is taken from the Viking 1 lander measurements, and consequently the wall temperature is adjusted to a value closer to the free-stream conditions and it is set to 150 K. The boundary conditions for the two cases for Mars atmosphere are summarized in Table 6. For this comparison between Earth and Mars, the selected GSI model is the Maxwellian with partially diffuse reflection ($\alpha_{acc} = 0.55$), VHS model for the intermolecular collisions, with no gas-phase reactions. The number density contour plot in Fig.13 of case 1 (Earth, 180 km) appears very similar to the one from case 8 (Mars, 140 km).

Table 5: Composition of the free-stream set as boundary conditions for each simulation for Martian atmosphere.

Case ID	h (km)	x_{CO_2} (-)	x_{O} (-)	x_{N_2} (-)	x_{CO} (-)	x_{Ar} (-)	x_{O_2} (-)
Case 8	140	0.8365	0.0650	0.0415	0.0360	0.0039	0.0171
Case 9	150	0.7984	0.0870	0.0570	0.0380	0.0026	0.0170

Table 6: Boundary conditions for the Mars atmosphere cases corresponding to the free-stream conditions.

Case ID	h (km)	ρ (kg m^{-3})	n_{tot} (m^{-3})	T (K)	p (Pa)	v_{in} (m s^{-1})
Case 8	140	1.1×10^{-9}	1.6×10^{16}	158	3.5×10^{-5}	3400
Case 9	150	4.5×10^{-10}	6.8×10^{15}	171	1.6×10^{-5}	3400

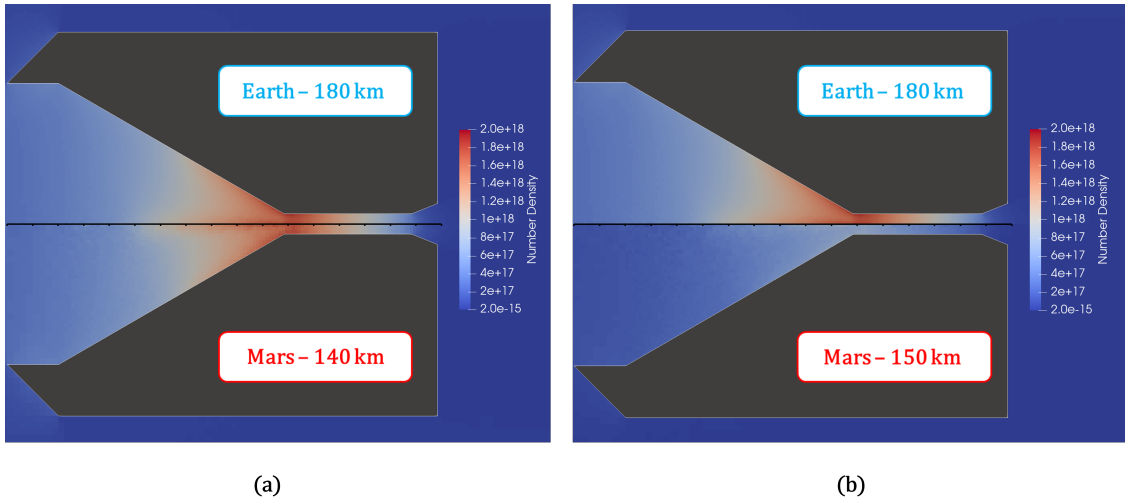


Figure 13: Contour plots of number density values for Martian atmosphere at 140 km (a) and 150 km (b) compared to Earth at 180 km.

The compression performance is reduced for the Mars cases: the pressure along the stagnation line is 50% less for case 8 and 80% less for case 9 if compared to case 1 from Earth as shown in Fig.14a). However, the design of the intake and collection stage is not optimized nor designed specifically for Mars applications, hence the addition of a molecular trap at the intake inlet, along with the design optimization might improve the compression performance. An analogous outcome is observed for the mass flux in Fig.14b), suggesting a design improvement.

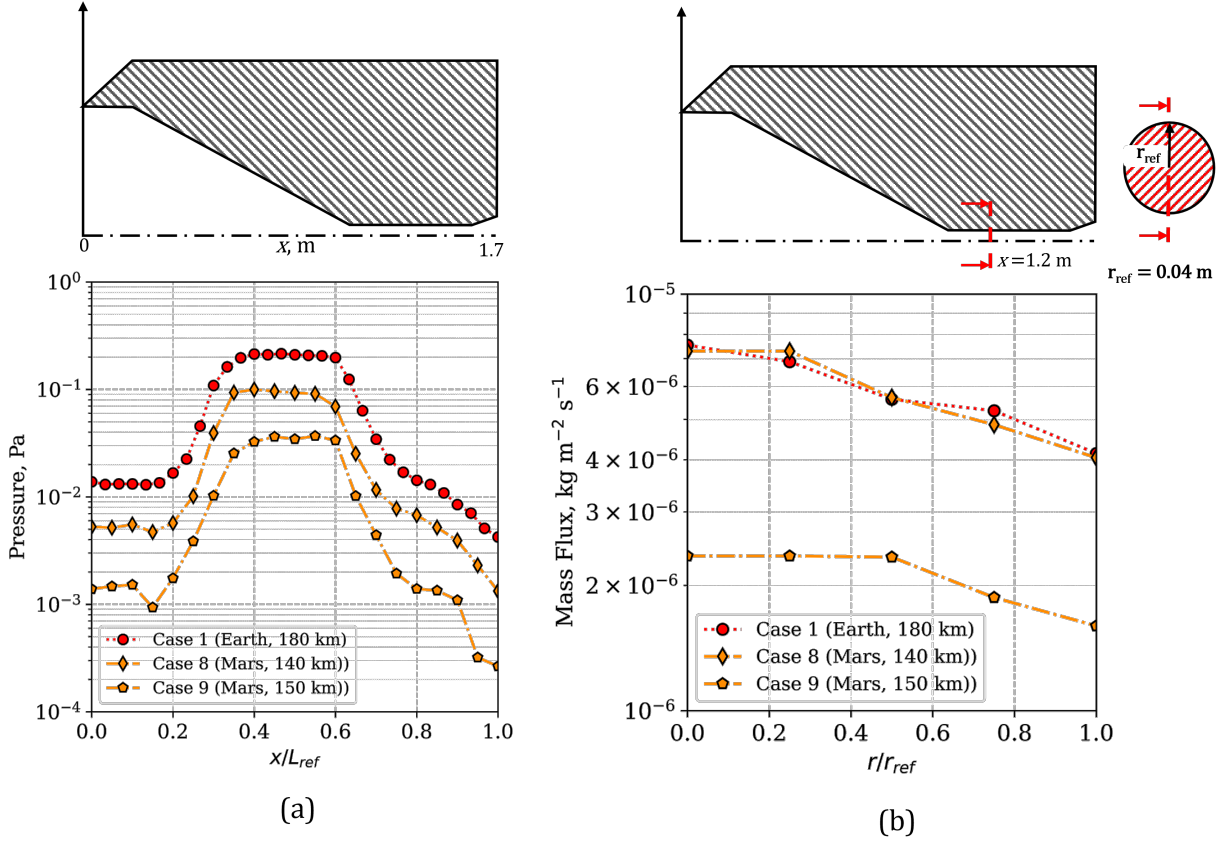


Figure 14: Pressure along the axi-symmetry axis (a), mass flux at the cross-section of the ionization stage inlet (b).

D. Drag force: Mars and Earth

One of the vital aspects of the ABEP design is the capacity to fully compensate the drag force. The theory behind the aerodynamic drag force for satellite applications has been extensively studied in literature,^{38,39} and in this study the aim is to provide a general estimation of the drag force from the DSMC simulations for the simple slope geometry for both Mars (140 km) and Earth (180 km). The aerodynamic drag force D is defined as in Eq.(5):

$$D = \frac{1}{2} c_d A_{ref} \rho v^2 \quad (5)$$

where A_{ref} is the reference area, v is the velocity of the incident atmospheric particles, hence the orbiting velocity, ρ is the free-stream density that varies with the altitude, and c_d is the drag coefficient. Since the A_{ref} is fixed by the geometry, v depends on the orbit type, ρ is estimated by the atmospheric characterization depending on the altitude, the only source of uncertainty for the drag estimation is the c_d , which can be treated as a fixed value, alternatively calculated by semi-empirical models, or determined by physical models. The DSMC simulations can directly calculate the value of D , without the need to set the value of the c_d a priori. In this study, as a final remark, the different drag forces for case 1 and case 8 are reported. First, the validation of this study framework is assessed by the comparison between case 1 and the reference case

from literature, which for the slope geometry is reported¹⁸ for the fully diffuse case ($\alpha_{acc}=1.0$). For the case with fully diffuse reflection, the drag resulting from the DSMC simulation from this study is ~ 34.2 mN, with a 1.15% error if compared to the reference case from literature¹⁸ (34.5983 mN). Moving to the case of partially diffuse reflection with Maxwellian model with the α_{acc} set to 0.55, the Earth case at 180 km (case 1) is characterized by a drag of ~ 29.7 mN, whereas for case 8 in Mars orbit at 140 km altitude the drag is ~ 12.5 mN. Hence, the drag from case 8 is $\sim 42\%$ of the one for Earth in case 1. Since A_{ref} if the same, a qualitative check on the DSMC results can be done by comparing the differences in the DSMC results by the the product $\rho \cdot v^2$: for case 1 is 31.303 N m^{-2} , for case 8 is 12.72 N m^{-2} , hence it is $\sim 40.6\%$ of case 1, which is reasonable in agreement with the $\sim 42\%$ from the simulations.

IV. Conclusion

Ground tests and numerical simulations can provide a synergic approach to tackle the design of ABEP for planetary and orbit specific missions, leading to reliable ABEP prototypes for future in-orbit demonstrations. In this study, a DSMC-based numerical framework is presented to achieve the characterization of collection and compression performances and drag estimation. The focus is on the impact of GSI models (specular, total and partially diffuse, and lobular reflection) with a brief check on the influence of the inter-particle collision models (VHS and VSS). Slight differences are observed between VHS (case 1) and VSS (case 2), as well as the inclusion of gas-phase reaction (case 3). As for the GSI model, the specular reflection (case 5) results in a higher compression performance, whereas the Maxwellian model (case 1) yields similar results to the CLL with an anisotropic scattering kernel (case 7), whereas different results are yielded by the CLL with isotropic kernel (case 6). Finally, the comparison between two Mars low-orbits and the Earth case at 180 km is presented. With the Maxwellian partially diffuse reflection, the case at 140 km (case 8) is comparable to the case 1 in terms of number density values, however the maximum pressure increase along the axi-symmetry line is 50% less than case 1 (Earth 180 km), but the aerodynamic drag force calculated by the DSMC method is 40% less for case 8 if compared to the case 1. After this comparison between Mars and Earth low orbit performance, further development in the design optimization could be the next required step.

Acknowledgments

A special thanks to Aloha Mingo and Pavel Smirnov for the fruitful discussions regarding the development of the atmosphere breathing electric propulsion systems.

References

- ¹A. Filatyev, A. Golikov, A. Erofeev, S. Khartov, A. Lovtsov, D. Padalitsa, V. Skvortsov, and O. Yanova, "Research and development of aerospace vehicles with air breathing electric propulsion: Yesterday, today, and tomorrow," *Progress in Aerospace Sciences*, vol. 136, p. 100877, 2023.
- ²T. Andreussi, E. Ferrato, and V. Giannetti, "A review of air-breathing electric propulsion: from mission studies to technology verification," *Journal of Electric Propulsion*, vol. 1, no. 1, p. 31, 2022.
- ³P. Zheng, J. Wu, Y. Zhang, and B. Wu, "A comprehensive review of atmosphere-breathing electric propulsion systems," *International Journal of Aerospace Engineering*, vol. 2020, pp. 1–21, 2020.
- ⁴K. Hohman, "Atmospheric breathing electric thruster for planetary exploration." Busek Co.Inc., 2012, vol. 11.
- ⁵D. Di Cara, J. G. Del Amo, A. Santovincenzo, B. C. Dominguez, M. Arcioni, A. Caldwell, and I. Roma, "Ram electric propulsion for low earth orbit operation: an esa study," in *30th international electric propulsion conference*, vol. 21, 2007, p. 22.
- ⁶K. Nishiyama, "Air breathing ion engine concept," in *54th International Astronautical Congress of the International Astronautical Federation, the International Academy of Astronautics, and the International Institute of Space Law*. American Institute of Aeronautics and Astronautics, 2003.
- ⁷M. Tagawa, K. Yokota, K. Nishiyama, H. Kuninaka, Y. Yoshizawa, D. Yamamoto, and T. Tsuboi, "Experimental study of air breathing ion engine using laser detonation beam source," *Journal of Propulsion and Power*, vol. 29, no. 3, pp. 501–506, 2013.
- ⁸T. Andreussi, E. Ferrato, C. Paisonni, A. Kitaeva, V. Giannetti, A. Piragino, S. Schäff, K. Katsonis, C. Berenguer, Z. Kovacova *et al.*, "The aether project: development of air-breathing electric propulsion for vleo missions," *CEAS space journal*, vol. 14, no. 4, pp. 717–740, 2022.
- ⁹F. Romano, T. Binder, G. Herdrich, S. Fasoulas, and T. Schönherr, "Intake design for an atmosphere-breathing electric propulsion system," *Space Propulsion*, vol. 2016, 2016.
- ¹⁰F. Romano, Y.-A. Chan, G. Herdrich, C. Traub, S. Fasoulas, P. Roberts, K. Smith, S. Edmondson, S. Haigh, N. Crisp

et al., “Rf helicon-based inductive plasma thruster (ipt) design for an atmosphere-breathing electric propulsion system (abep),” *Acta Astronautica*, vol. 176, pp. 476–483, 2020.

¹¹F. Romano, J. Espinosa-Orozco, M. Pfeiffer, G. Herdrich, N. H. Crisp, P. Roberts, B. Holmes, S. Edmondson, S. Haigh, S. Livadiotti *et al.*, “Intake design for an atmosphere-breathing electric propulsion system (abep),” *Acta Astronautica*, vol. 187, pp. 225–235, 2021.

¹²N. H. Crisp, P. C. Roberts, S. Livadiotti, V. T. A. Oiko, S. Edmondson, S. Haigh, C. Huyton, L. Sinpetru, K. Smith, S. Worrall *et al.*, “The benefits of very low earth orbit for earth observation missions,” *Progress in Aerospace Sciences*, vol. 117, p. 100619, 2020.

¹³L. Wu, *Rarefied gas dynamics: kinetic modeling and multi-scale simulation*. Springer Nature, 2022.

¹⁴G. A. Bird, *Molecular gas dynamics and the direct simulation of gas flows*. Oxford university press, 1994.

¹⁵S. Fasoulas, C.-D. Munz, M. Pfeiffer, J. Beyer, T. Binder, S. Copplestone, A. Mirza, P. Nizenkov, P. Ortwein, and W. Reschke, “Combining particle-in-cell and direct simulation monte carlo for the simulation of reactive plasma flows,” *Physics of Fluids*, vol. 31, no. 7, p. 072006, 07 2019.

¹⁶C. Rapisarda, P. C. Roberts, and K. L. Smith, “Design and optimisation of a passive atmosphere-breathing electric propulsion (abep) intake,” *Acta Astronautica*, vol. 202, pp. 77–93, 2023.

¹⁷X. Jin, X. Cheng, Y. Huang, Q. Wang, B. Wang, and Q. Shen, “Numerical analysis of inlet flows at different altitudes in the upper atmosphere,” *Physics of Fluids*, vol. 35, no. 9, 2023.

¹⁸X. Jin, W. Miao, X. Cheng, Q. Wang, and B. Wang, “Monte carlo simulation of inlet flows in atmosphere-breathing electric propulsion,” *AIAA Journal*, vol. 62, no. 2, pp. 518–529, 2024.

¹⁹P. Zheng, J. Wu, Y. Zhang *et al.*, “Design and numerical investigation on the intake of atmosphere-breathing electric propulsion,” *Acta Astronautica*, vol. 188, pp. 215–228, 2021.

²⁰J. C. Maxwell, “VII. on stresses in rarified gases arising from inequalities of temperature,” *Philosophical Transactions of the royal society of London*, no. 170, pp. 231–256, 1879.

²¹C. Cercignani and M. Lampis, “Kinetic models for gas-surface interactions,” *Transport theory and statistical physics*, vol. 1, no. 2, pp. 101–114, 1971.

²²R. Lord, “Some extensions to the cercignani–lampis gas–surface scattering kernel,” *Physics of Fluids A: Fluid Dynamics*, vol. 3, no. 4, pp. 706–710, 1991.

²³J. M. Picone, A. E. Hedin, D. P. Drob, and A. C. Aikin, “Nrlmsise-00 empirical model of the atmosphere: Statistical comparisons and scientific issues,” *Journal of Geophysical Research: Space Physics*, vol. 107, no. A12, pp. SIA 15–1–SIA 15–16, 2002.

²⁴P. Crandall and R. E. Wirz, “Air-breathing electric propulsion: mission characterization and design analysis,” *Journal of Electric Propulsion*, vol. 1, no. 1, p. 12, 2022.

²⁵A. Seiff and D. B. Kirk, “Structure of the atmosphere of mars in summer at mid-latitudes,” *Journal of Geophysical Research*, vol. 82, no. 28, pp. 4364–4378, 1977.

²⁶S. Haider and K. Mahajan, “Lower and upper ionosphere of mars,” *Space Science Reviews*, vol. 182, no. 1, pp. 19–84, 2014.

²⁷R. C. Blanchard, R. G. Wilmoth, and J. N. Moss, “Aerodynamic flight measurements and rarefied-flow simulations of mars entry vehicles,” *Journal of Spacecraft and Rockets*, vol. 34, no. 5, pp. 687–690, 1997.

²⁸C. Justus, B. James, S. Bougher, A. Bridger, R. Haberle, J. Murphy, and S. Engel, “Mars-gram 2000: A mars atmospheric model for engineering applications,” *Advances in Space Research*, vol. 29, no. 2, pp. 193–202, 2002.

²⁹J. Schofield, J. R. Barnes, D. Crisp, R. M. Haberle, S. Larsen, J. Magalhaes, J. R. Murphy, A. Seiff, and G. Wilson, “The mars pathfinder atmospheric structure investigation/meteorology (asi/met) experiment,” *Science*, vol. 278, no. 5344, pp. 1752–1758, 1997.

³⁰C. A. Barth, A. Stewart, C. Hord, and A. Lane, “Mariner 9 ultraviolet spectrometer experiment: Mars airglow spectroscopy and variations in lyman alpha,” *Icarus*, vol. 17, no. 2, pp. 457–468, 1972.

³¹C. A. Barth, “The atmosphere of mars,” *Annual Review of Earth and Planetary Sciences*, vol. 2, no. 1, pp. 333–367, 1974.

³²A. O’Nier and M. B. McElroy, “Composition and structure of mars’ upper atmosphere: Results from the neutral mass spectrometers on viking 1 and 2,” *Journal of Geophysical Research*, vol. 82, no. 28, pp. 4341–4349, 1977.

³³P. R. Mahaffy, M. Benna, M. Elrod, R. V. Yelle, S. W. Bougher, S. W. Stone, and B. M. Jakosky, “Structure and composition of the neutral upper atmosphere of mars from the maven ngims investigation,” *Geophysical research letters*, vol. 42, no. 21, pp. 8951–8957, 2015.

³⁴R. J. Lillis, D. A. Brain, S. W. Bougher, F. Leblanc, J. G. Luhmann, B. M. Jakosky, R. Modolo, J. Fox, J. Deighan, X. Fang *et al.*, “Characterizing atmospheric escape from mars today and through time, with maven,” *Space Science Reviews*, vol. 195, pp. 357–422, 2015.

³⁵S. Plimpton, S. Moore, A. Borner, A. Stagg, T. Koehler, J. Torczynski, and M. Gallis, “Direct simulation monte carlo on petaflop supercomputers and beyond,” *Physics of Fluids*, vol. 31, no. 8, 2019.

³⁶M. Pfeiffer, “An optimized collision-averaged variable soft sphere parameter set for air, carbon, and corresponding ionized species,” *Physics of Fluids*, vol. 34, no. 11, 2022.

³⁷C. Park, J. Howe, R. Jaffe, and G. Candler, “Chemical-kinetic problems of future nasa missions,” in *29th Aerospace Sciences Meeting*, 1991, p. 464.

³⁸K. Moe and M. M. Moe, “Gas–surface interactions and satellite drag coefficients,” *Planetary and Space Science*, vol. 53, no. 8, pp. 793–801, 2005.

³⁹P. M. Mehta, R. Linares, and E. K. Sutton, “Data-driven inference of thermosphere composition during solar minimum conditions,” *Space Weather*, vol. 17, no. 9, pp. 1364–1379, 2019.